SCIENCE CHINA
Information Sciences

• **Supplementary File** •

Fully Coupled Electrothermal Simulation of Resistive Random Access Memory (RRAM) Array

Da-Wei WANG[1], Wen-Sheng ZHAO[2], Wenchao CHEN[1,3], Hao XIE[1] & Wen-Yan YIN[1*]

[1]*College of ISEE, Zhejiang University, Hangzhou* 310058*, China;*
[2]*School of Electronics and Information, Hangzhou Dianzi University, Hangzhou* 310018*, China;*
[3]*ZJU-UIUC Institute, International Campus, Zhejiang University, Hangzhou* 314400*, China*

Appendix A Numerical strategy

The electrothermal process taken place in a RRAM consists of ion migration, current transport, and thermal conduction. The electrical simulation can be performed by solving the ion transport equation and current continuity equation, *i.e.*

$$\nabla \cdot \left(\mu(T) n_D \overrightarrow{E} - D(T)\nabla n_D\right) = \frac{\partial n_D}{\partial t} + RG \tag{A1}$$

$$\nabla \cdot (\sigma(T)\nabla V) = 0 \tag{A2}$$

where V is the voltage, T is the local temperature, $\overrightarrow{E} = -\nabla V$ is the electric field, $\mu(T)$ is the temperature-dependent mobility, n_D is the ion concentration, and RG is the generation/recombination rate. $\sigma(T)$ is temperature-dependent electrical conductivity, and for the doped HfO_2, we have [1]

$$\sigma(T) = \sigma_0(n_D)\, exp\left(-\frac{E_{AC}}{k_B T}\right) \tag{A3}$$

where k_B is the Boltzmann's constant and E_{AC} is the activation energy for conduction. $\sigma_0(n_D)$ is the pre-exponential factor, and it is ion density-dependent. The ion diffusion coefficient $D(T)$ is temperature activated according to the Arrhenius law [1]

$$D(T) = D_0 exp\left(-\frac{E_{AC}}{k_B T}\right) \tag{A4}$$

where D_0 is the diffusion coefficient at $T_0 = 300K$.

The thermal analysis is conducted by solving the following governing equation

$$\rho C_p(T)\frac{\partial T}{\partial t} = \kappa(T)\nabla^2 T + Q \tag{A5}$$

where $C_p(T)$ and $\kappa(T)$ are the temperature-dependent heat capacity and thermal conductivity of the materials, respectively. A nonlinear thermal conductivity model for HfOx is specified as [2]

$$\kappa_{HfO} = \kappa_{HfO0}(n_D)(1 + \lambda(T - T_0)) \tag{A6}$$

where $\lambda = 0.01$ is the linear thermal coefficient. $\kappa_{HfO0}(n_D)$ is the thermal conductivity at $T_0 = 300K$, and it is a function of doping concentration [3].

It is worth noting that material parameters in (A1), (A2) and (A5) are temperature-dependent, thereby providing links between electric and thermal fields during electrothermal co-simulation. The material parameters used here are summarized in Table A1.

* Corresponding author (email: wyyin@zju.edu.cn)

Table A1 Physical parameters of the involved materials

Comp.	Materials	Physical parameters
B/W Line	Pt	$\kappa_{Pt} = 71.6W/(m \cdot K)$
		$\sigma_{Pt} = 8.9 \times 10^6 S/m$
		$C_{Pt} = 131.4J/Kg \cdot \circ C$
	PGEC [4,5]	$\kappa_{PE} = 0.5W/(m \cdot K)$
		$\sigma_{Pt} = 6.8 \times 10^6 S/m$
CF	HfO_2	$\kappa_{CF} : Eq.(6)$
		$\sigma_{CF} : Eq.(3)$
		$C_{Pt} = 445J/Kg \cdot \circ C$
Dioxide	HfO_2	$\kappa_{ox} = 0.5W/(m \cdot K)$
		$\sigma_{ox} : Eq.(3)$
		$C_{ox} = 445J/Kg \cdot \circ C$
High κ Insulator	Si_3N_4 [6]	$\kappa_{SiN} = 0.02W/(m \cdot K)$
		$\sigma_{SiN} = 1.0 \times 10^{-10} S/m$
		$C_{SiN} = 710J/Kg \cdot \circ C$
Selector	poly-Si	$\kappa_s = 11.7W/(m \cdot K)$
		$\sigma_s = 2.07 \times 10^6 S/m, on - state$
		$\sigma_s = 2.0 \times 10^- 2S/m, off - state$
		$C_s = 133J/Kg \cdot \circ C$

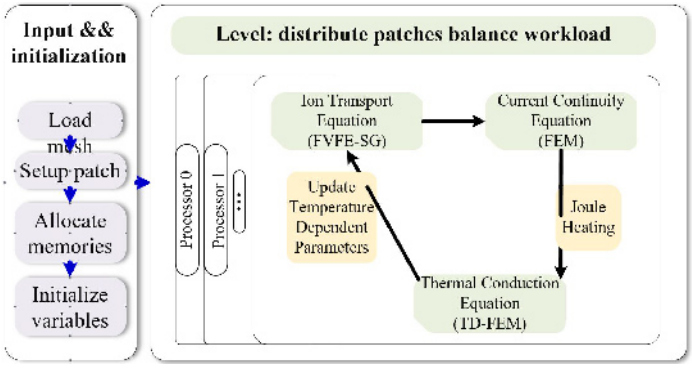

Figure A1 Hierarchical structure of the developed parallel simulator.

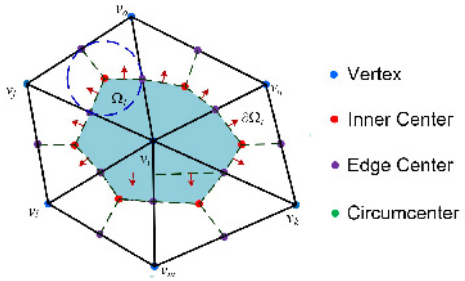

Figure A2 The control volume cell ω_i around vertex v_i for triangle meshing grid.

Figure A1 outlines the hierarchical structure of the in-house developed parallel simulator. As stated in the figure, the geometric model, as well as input information, is loaded at first and then the JANMIN evenly divides the whole model into distributed patches using the METIS software package [7]. After that, each patch is assigned to one process according to the inherent workload distribution scheme. To balance the workloads and dynamically minimize the number of successive subdomains allocated to each process, massage passing interface (MPI) parallel programming scheme is utilized. On each patch, the ion transport equation and current continuity equation are solved and subsequently, the heat generation rate is calculated as the source in heat conduction equation. During this process, the FEM is employed to discretize the current

continuity and heat conduction equations, while the FVFE-SG method is implemented for the ion migration governing equation [8]. A HYPER-PCG solver is utilized to solve the system matrix equation on each patch.

Following, the implementation of the FVFE-SG method over control volume cell ω_i shown in Figure A2 are addressed below. The governing equation (A1) is integrated over the volume cell ω_i

$$\frac{1}{q}\int_{\Omega_i}\nabla\cdot\overrightarrow{J}d\Omega=\int_{\Omega_i}\frac{\partial n_D}{\partial t}d\Omega+\int_{\Omega_i}Rd\Omega \tag{A7}$$

The Divergence theorem is applied to the left-hand side of (A7) to obtain its weak form, *i.e.*

$$\frac{1}{q}\int_{\Omega_i}\left(\overrightarrow{J}\cdot\overrightarrow{n}\right)dS=\int_{\Omega_i}\frac{\partial n}{\partial t}d\Omega+\int_{\Gamma_N}hdS+\int_{\Omega_i}Rd\Omega \tag{A8}$$

where $\partial\omega_i$ is the boundary of ω_i. By involving the standard Lagrangian basis N, the particle density within each mesh element can be expanded as

$$n=\sum_{m\in\Omega_{tri}\cup\Gamma_N}n_{D,m}N_m+\sum_{m\in\Gamma_D}n_{D,m}(t)N_m \tag{A9}$$

where $limits_{m\in\Omega_{tri}\cup\Gamma_N}$ denotes that the vertex v_m is in the interior of calculated domain or on the Neumann boundary, $limits_{m\in\Gamma_D}$ denotes that the vertex v_m belongs to the Dirichlet boundary, and $n_{D,m}(t)$ is the time-dependent Dirichlet boundary value at the vertex v_m. As shown in Figure A2, the control volume cell around the vertex v_i is composed of five parts belonging to five different mesh grids. To describe the problem more clearly, the integration over the part in mesh cell δ_{ijo} will be elaborated in the following.

With the consideration of the upwind effect, the current density $\overrightarrow{J}$ described in (A8) should be modified to SG formulation at each edge of the mesh cell. The SG formulation along the edge e_ij is expressed as

$$\left|\overrightarrow{J}_{ij}\right|=\frac{\mu_nE_{ij}}{2}\left(n_{D,j}\left[\coth\left(a_{ij}\right)+1\right]-n_{D,i}\left[\coth\left(a_{ij}\right)-1\right]\right) \tag{A10}$$

where a_ij is the Reynolds number along the edge e_ij, and it can be calculated by $a_{ij}=\mu_nE_{ij}l_{ij}/(2D_n)$. l_ij is the length of edge e_ij, and E_ij is the electric field intensity on edge e_ij. As mentioned above, the edge current is no longer perpendicular to the adjacent segment of boundary $\partial\omega_i$ in the proposed FVFEM-SG. To get the outward norm, the Nedelec edge basis space is employed to interpolate the upwind edge current in (A10) to the center of adjacent segment of boundary $\partial\omega_i$ by

$$\overrightarrow{J}=\sum_{e_{mp}\in E(\Delta_{ijo})}\left|\overrightarrow{J}_{mp}\right|\cdot\overrightarrow{W}_{mp} \tag{A11}$$

By substituting (A9)-(A11) into (A8), the integration over the area $\Delta_{ijo}\cap\partial\Omega_i$ can be obtained as

$$\begin{aligned}&\sum_{m\in\Delta_{ijo}}\frac{\partial n_{D,m}(t)}{\partial t}\int_{\Delta_{ijo}\cap\Omega_i}N_md\Omega\\&-\sum_{e_{mp}\in E(\Delta_{ijo})}\frac{\mu_nE_{ij}}{2}\left(n_{D,j}\left[\coth\left(a_{ij}\right)+1\right]-n_{D,i}\left[\coth\left(a_{ij}\right)-1\right]\right)\cdot\int_{\Delta_{ijo}\cap\partial\Omega_i}\overrightarrow{W}_{mp}\cdot\overrightarrow{n}dS\\&=-\int_{\Gamma_N}hdS-\int_{\Delta_{ijo}\cap\Omega_i}Rd\Omega\end{aligned} \tag{A12}$$

Although the second term in the left-hand side of (A12) is over the edges, it operates on the node degree of freedoms. Therefore, (A12) can be further simplified by rewriting the second term as double sum, *i.e.*

$$\begin{aligned}&\sum_{m\in\Delta_{ijo}}\frac{\partial n_{D,m}(t)}{\partial t}\int_{\Delta_{ijo}\cap\Omega_i}N_md\Omega\\&-\sum_{m\in\Delta_{ijo}}n_{D,p}\sum_{e_{mp}\in E(\Delta_{ijo})}\sigma_{mp}\frac{\mu_nE_{mp}}{2}\left(\coth\left(a_{mp}\right)-\sigma_{mp}\right)\cdot\int_{\Delta_{ijo}\cap\partial\Omega_i}\overrightarrow{W}_{mp}\cdot\overrightarrow{n}dS\\&=-\int_{\Gamma_N}hdS-\int_{\Delta_{ijo}\cap\Omega_i}Rd\Omega\end{aligned} \tag{A13}$$

where $\sigma_{mp}=-1$ if e_mp is oriented from v_m to v_p, and $\sigma_{mp}=1$ if e_mp is oriented in the opposite direction. By calculating (A13) at all vertices in the mesh cell δ_ijo, the matrix form of (A13) can be derived as

$$[M_e]\frac{\partial}{\partial t}\{n_D\}-[K_e]\{n_D\}=\{f_e\} \tag{A14}$$

where K_e is the upwind stiffness matrix and its element can be calculated by

$$K_{e,ip}=\sum_{e_{mp}\in E(\Delta_{ijo})}\sigma_{mp}\frac{\mu_nE_{mp}}{2}\left(\coth\left(a_{mp}\right)-\sigma_{mp}\right)\cdot\int_{\Delta_{ijo}\cap\partial\Omega_i}\overrightarrow{W}_{mp}\cdot\overrightarrow{n}dS \tag{A15}$$

M_e is the damping matrix and its element can be calculated by

$$M_{e,ip} = \int_{\Delta_{ijo} \cap \Omega_i} N_p d\Omega \tag{A16}$$

f_e is the column vector and its element can be calculated by

$$f_{e,i} = -\int_{\Gamma_N} h dS - \int_{\Delta_{ijo} \cap \Omega_i} R d\Omega \tag{A17}$$

Using the backward difference with respect to time, (A14) can be discretized as

$$([M_e] - \Delta t\,[K_e])\,\{n_D\}_{t+\Delta t} = [M_e]\,\{n_D\}_t + \Delta t\,\{f_e\} \tag{A18}$$

where δ_t is the time step for time evolution. The system equation for the problem domain can be obtained by summing (A18) over all elements as

$$([M] - \Delta t\,[K])\,\{n_D\}_{t+\Delta t} = [M]\,\{n_D\}_t + \Delta t\,\{f\} \tag{A19}$$

where K is the system upwind stiffness matrix, and M is the system damping matrix. This procedure can be easily extended to solve 3-D problems by replacing the control volume in Figure A2 with the control volume composed of tetrahedron inner center, inner center of surface triangular, and center of edge in 3-D mesh cells. For steady-state case, the time-dependent term can be removed,

$$-[K]\,\{n_D\} = \{f\} \tag{A20}$$

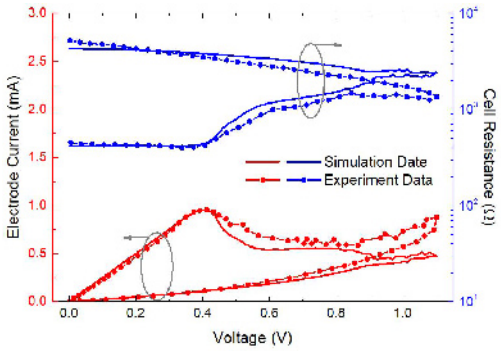

Figure A3 Measured and simulated I-V and R-V characteristics of RRAM cell with 14 nm CF diameter and 20 nm CF height. The voltage is increased according to a triangular sweep with $1.1V/s$ ramp rate.

To assess the internal simulator, the electrothermal characteristics of a 1R RRAM cell with CF diameter of 14 nm and height of 20 nm is simulated and the results are compared with measured data presented in [3]. As shown in Figure A3, the calculated and measured data match well.

Appendix B Dimensional parameters of CGVRRAM array

The dimensional parameters of the proposed CGVRRAM cell and array are listed in Table B1.

Table B1 Physical parameters of the involved materials

Parameter	Definition	Value
w_{cbar}	Dimension of vertical bar	60 nm
w_{line}	Width of word line and bit line	176 nm
h_{line}	Height of word line and bit line	20 nm
h_s	Height of selector	40 nm
w_{cell}	Width of RRAM cell	40 nm
h_{cell}	Height of RRAM cell	90 nm
h_{cf}	Height of CF	40 nm
r_{cf}	CF radius	4 nm
t_{ch}	Thickness of channel	10 nm
t_{gins}	Thickness of gate insulator layer	3 nm
w_{getd}	Width of cross-gate line	20 nm
h_{getd}	Height of cross-gate line	20 nm
w_{gap}	The space between memory chains	30 nm
h_{tins}	Thickness of the insulator gap layer	20 nm

Appendix B.1 Electrothermal characteristics of CGVRRAM array

The reset process of a CGVRRAM cell is activated by applying a triangular voltage pulse with $1V/s$ ramp and $0.5V$ amplitude to the top boundary of the poly-Si channel. The temperature and ion density distributions of the cell at $t = 0.5s$ are illustrated in Figure B1, where the ion density at the hot spot is extremely low.

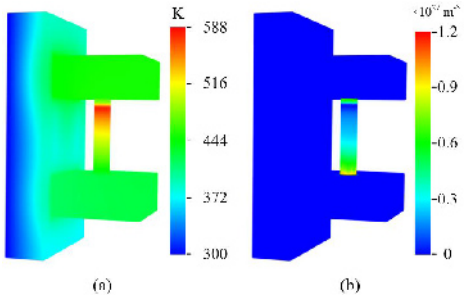

Figure B1 (a) Temperature and (b) ion density distributions in the CGVRRAM cell at $t = 0.5s$.

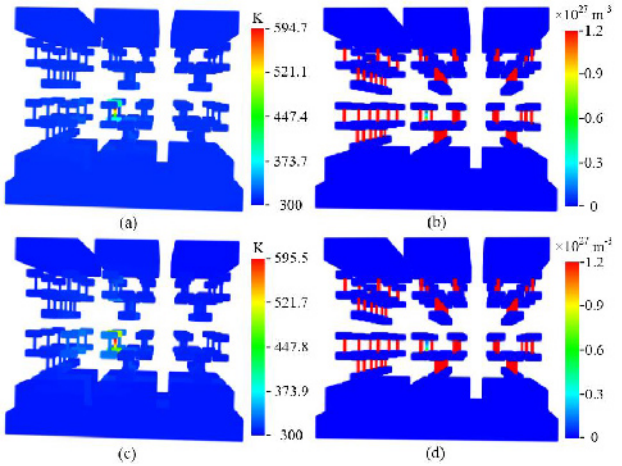

Figure B2 (a) Temperature and (b) ion density distributions of the CGVRRAM array with SiO_2 dielectric components at $t = 0.5s$; (c) temperature and (d) its ion density distributions with Si_3N_4 dielectric components at $t = 0.35s$.

Then, the electrothermal characterization of the CGVRRAM array composed of 18 units (*i.e.*, 72 cells) is conducted. Similarly, two cases are considered where SiO_2 and Si_3N_4 are used as dielectric components, respectively. The temperature and ion density distributions of the CGVRRAM arrays in two cases are shown in Figures B2. It is found that the thermal crosstalk effects in both cases are acceptable, as they have negligible influences on the electrical performances of the victim cells.

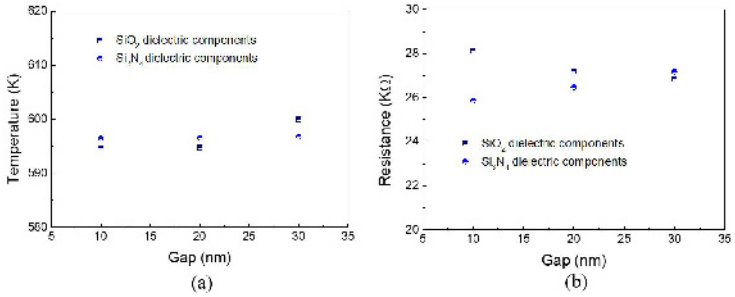

Figure B3 (a) The maximum temperature and (b) cell resistance of programmed cells in both arrays with SiO_2 and Si_3N_4 dielectric components.

After that, the impacts of w_{gap} on the maximum temperature and cell resistance are investigated, as shown in Figure B3. It is found that the maximum temperature in the CGVRRAM array with SiO_2 dielectric components increases slightly

with the increasing w_{gap}, and it becomes almost unchanged when SiO_2 is replaced with Si_3N_4. The cell resistances in two cases are stable, as shown in Figure B3(b), indicating that the gap between memory chains has small influence on electrical and thermal performances of the CGVRRAM array. In the other word, the integration density of the proposed CGVRRAM array can be improved by reducing the w_{gap} reasonably.

As technology scaling is always desirable due to lower cost for unit storage space, the electrothermal characteristics of scaled CGVRRAM arrays with Si_3N_4 dielectric components are also examined. It is assumed that the scaling factor sweeps from 1.0 to 2.0. The temperature and ion density distributions in the CGVRRAM arrays with different scaling factors are shown in Figure B4 and Figure B5, respectively. It indicates that the thermal crosstalk effects in all cases are acceptable, as they have negligible influences on the electrical performances of the victim cells.

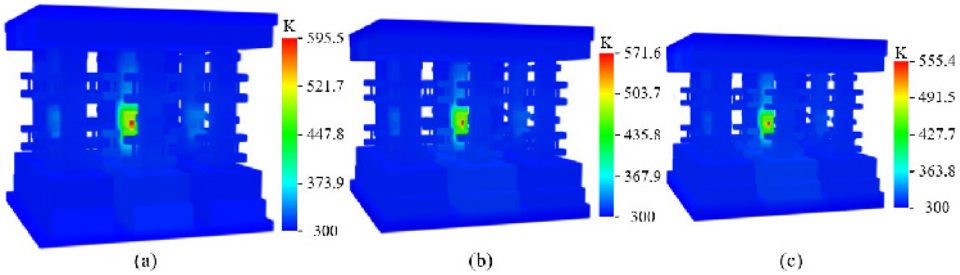

Figure B4 The temperature distributions in CGVRRAM arrays with different scaling factors at $t = 0.35s$. (a) $s_{coe} = 1.0$, (b) $s_{coe} = 1.5$, and (c) $s_{coe} = 2.0$.

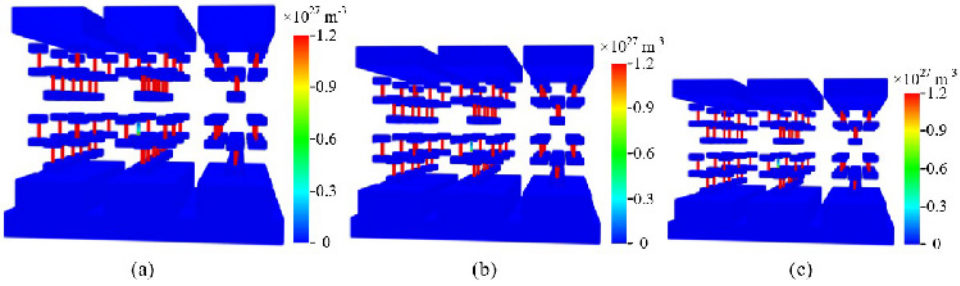

Figure B5 The ion density distributions in CGVRRAM arrays with different scaling factors at $t = 0.35s$. (a) $s_{coe} = 1.0$, (b) $s_{coe} = 1.5$, and (c) $s_{coe} = 2.0$.

Appendix C Electrothermal simulation of RRAM Array

Geometrically, crossbar structure consisting of single resistor (1R) cell or single selector-one resistor (1S1R) cell is one of the common RRAM array architecture, as shown in Figure C1. In Figure C1(c), a crossbar RRAM (CRRAM) array consisting of 54 1S1R cells ($4 \times 4 \times 3$)is shown, and for convenience, the cells in the array are marked by $xyz(i; j; k)$, where $i, j = 1, 2, 3, 4$, and $k = 1, 2, 3$.

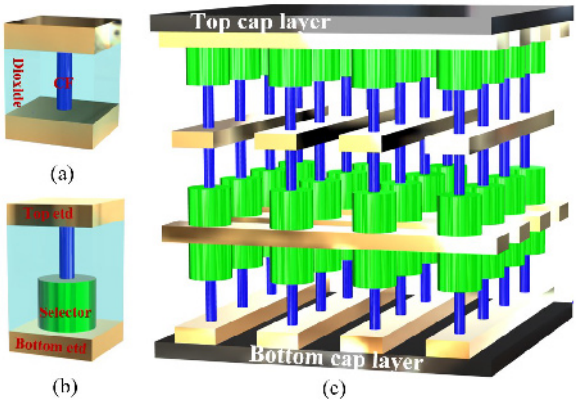

Figure C1 3-D views of (a) single resistor cell (1R), (b) single selector-one resistor cell (1S1R), and (c) crossbar RRAM array (CRRAM).

In the highly integrated RRAM array, thermal crosstalk effect between adjacent cells would influence the cell performance and reliability. Here, the electrothermal properties of RRAM cell and array are studied using the internal simulator, with the geometrical parameters listed in Table C1 [9–11] and physical parameters given in Table A1 adopted. As shown in Figure C1(c), the top and bottom surfaces of the RRAM array are attached with cap layers, while $T_0 = 300K$ is assigned to the outer boundaries of the cap layers.

Table C1 Physical parameters of the involved materials

Parameter/Entity	CF/Oxide	Selector	Bit/Word Line
Radius/Width(nm)	$r_{cf} = 5$	$w_{selector} = 40$	$w_{line} = 40$ $l_{line} = 60$
Height(nm)	$h_{cf} = 40$	$h_{selector} = 50$	$h_{line} = 30$

Appendix C.1 Electrothermal characteristics of 1S1R cell

The electrothermal characteristics of the 1S1R cell shown in Figure C1(b) are simulated. In the simulation, the selector is modeled as a cylinder. For selectors in the ON and OFF states, the equivalent electrical and thermal parameters are deduced from the I-V curve and materials of MOS device [12]. A triangular voltage pulse with 1 V/s ramp and 0.5 V amplitude is applied to the top electrode. The maximum temperature and cell resistance of the 1S1R RRAM cell as a function of biasing voltage are plotted in Figure C2, with their 3-D distributions shown in Figure C3.

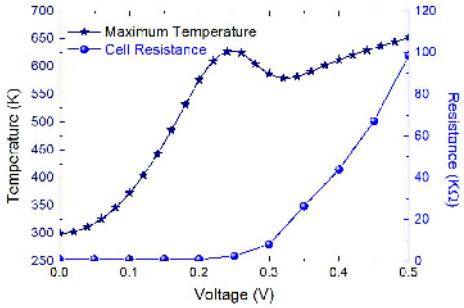

Figure C2 The maximum temperature and cell resistance of the 1S1R RRAM cell as a function of biasing voltage.

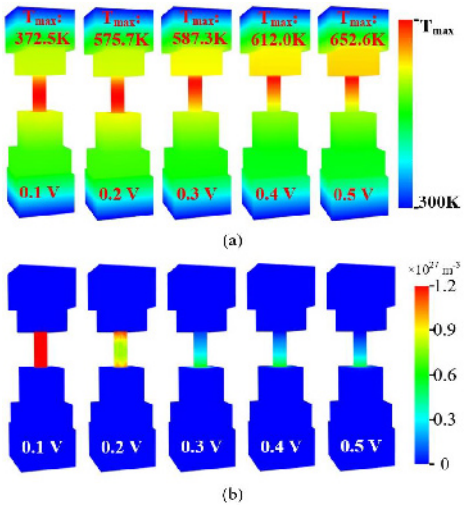

Figure C3 (a) Temperature and (b) ion density distributions of the 1S1R RRAM cell at different times.

It can be seen in Figure C2 that the cell resistance stays almost unchanged before the biasing voltage exceeds 0.2 V. After that, the cell resistance increases with an increasing growth rate with the biasing voltage. The ion density distributions shown in Figure C3(b) indicate that the ion density of CF starts to corrode at 0.2 V, and the break point widens with biasing voltage. Moreover, a drop in the maximum temperature is observed in Figure C2. This is mainly because the hot spot in the RRAM cell moves toward the top electrode as the biasing voltage increases. As the hot spot reaches the top electrode, the heat dissipation rate becomes greater than heat generation rate, thereby leading to a sudden drop in the

thermal resistance. The relationship between the heat generation rate and heat dissipation rate becomes inverted as the biasing voltage exceeds 0.33 V, and the maximum temperature starts to increase.

Appendix C.2 Electrothermal characteristics of CRRAM array

Further, the thermal crosstalk effect in a $4 \times 4 \times 3$ CRRAM array is investigated. In the real cases, the geometry of the CFs can be affected by the manufacturing process. Here, the effect of the major to minor axes ratio (ab_{ratio}) of the elliptic cylindrical CF on thermal crosstalk is examined. In all simulations, the cross-section area of CFs is invariant, and only the cell $xyz(2;2;2)$ is programmed by a triangular voltage pulse with 1 V/s ramp and 0.5 V amplitude. The 3-D temperature distributions of the CRRAM arrays with ab_{ratio} of 1, 2, and 3 are plotted in Figure C4. It is evident that the victim cells sharing electrode with the programmed cell are mostly influenced. Figures C5(a) and C5(b) show the temperature profiles along the symmetry axes of cells $xyz(2:3;2:3;1:3)$ at $t = 0.35s$. It is evident that the cells $xyz(2;2;3)$ and $xyz(2;3;2:3)$ exhibit much higher crosstalk temperatures than other victims, which is due to low thermal resistance of the sharing electrode. Moreover, it is found that the maximum temperature in CRRAM array increases as ab_{ratio} increases.

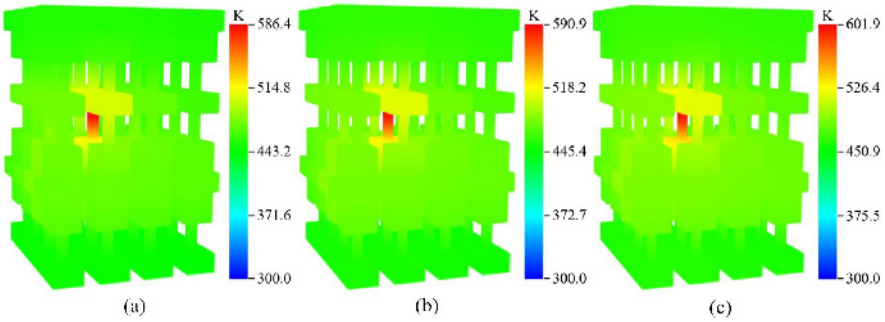

Figure C4 3-D temperature distributions in the CRRAM arrays at $t = 0.35s$. (a) $ab_{ratio} = 1$; (b) $ab_{ratio} = 2$; (c) $ab_{ratio} = 3$.

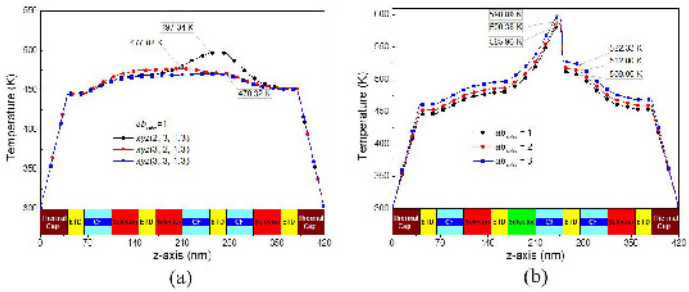

Figure C5 Temperature distributions along the symmetry axes of cells $xyz(2:3;2:3;1:3)$ at $t = 0.35s$. (a) $xyz(2;3;1:3)$, and $xyz(3;2:3;1:3)$; (b) $xyz(2;2;1:3)$.

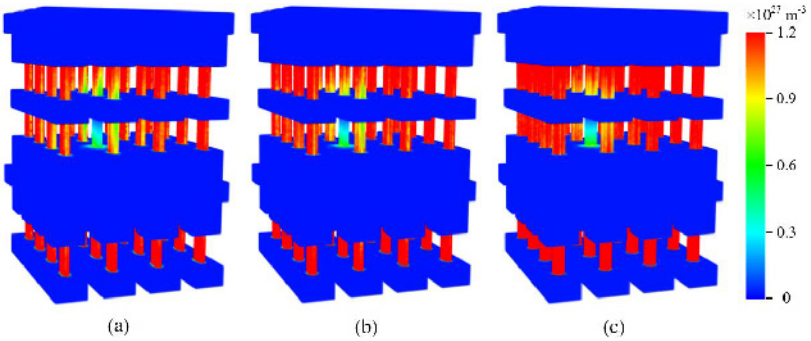

Figure C6 3-D ion density distributions in the CRRAM arrays at $t = 0.35s$. (a) $ab_{ratio} = 1$; (b) $ab_{ratio} = 2$; (c) $ab_{ratio} = 3$.

Figures C6(a)-(c) illustrate the ion density distributions in the CRRAM arrays with different ab_{ratio}, where the ion density distributions of cells adjacent to the programmed cell are highly distorted, especially the cells sharing word line

with the programmed one. This is consistent with the temperature distributions in Figure C4. The resistances of the RRAM cells $xyz(2:3;2:3;2:3)$ are depicted in Figure C7. It is evident that the cell resistances increase as ab_{ratio} increases. The main reasons are: (i) higher cell temperature and (ii) larger ellipse perimeter in cell with larger ab_{ratio}. It can be concluded that the carrier diffusion of the CF with larger ab_{ratio} is more susceptible to the temperature variation.

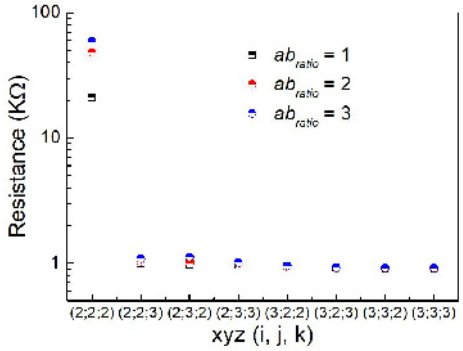

Figure C7 RRAM cell resistances in the CRRAM array at $t = 0.35s$.

Appendix C.3 Thermal resistance architecture

To mitigate the thermal crosstalk, an improvement in array architecture is proposed. Here, high thermal resistance layers (e.g., Si_3N_4 thin films) are inserted between adjacent cells to stop heat transfer between them. That is, each cell in the array is coated with a high resistance box. Moreover, the bit/word lines are replaced by the phonon glass and electron crystal (PGEC), which possesses both low thermal conductivity and high electrical conductivity [4, 5].

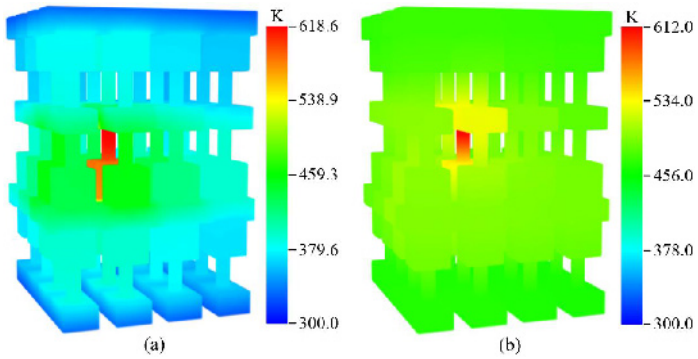

Figure C8 3-D temperature distributions in the CRRAM arrays (a) with high thermal resistance box at $t = 0.12s$ and (b) with no high thermal resistance box at $t = 0.4s$.

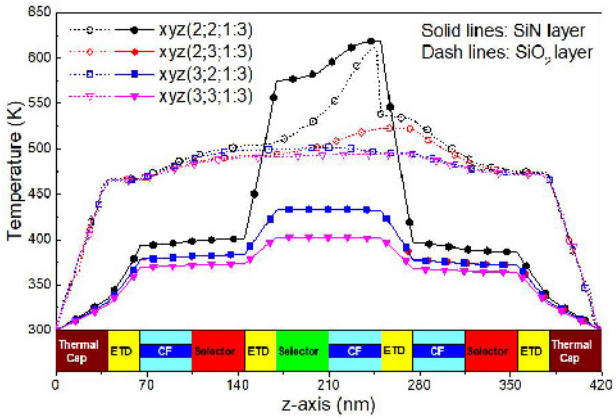

Figure C9 Temperature profiles along symmetry axes of cells $xyz(2:3;2:3;1:3)$.

Figures C8(a) and C8(b) show the simulated temperature distributions in the CRRAM arrays with and with no high thermal resistance box, respectively, and the temperature profiles along the symmetry axes of cells $xyz(2:3;2:3;1:3)$ are extracted and plotted in Figure C9. It is found that the implementation of high thermal resistance box can effectively suppress thermal crosstalk as well as programming voltage. This implies that the proposed design is beneficial to low power applications. Figures C10(a) and C10(b) show the ion density distributions in the CRRAM arrays with and with no high thermal resistance box, respectively. It is evident that the ion densities of the victim cells in the proposed design are rarely affected, while they are distorted to varying degrees in the original one.

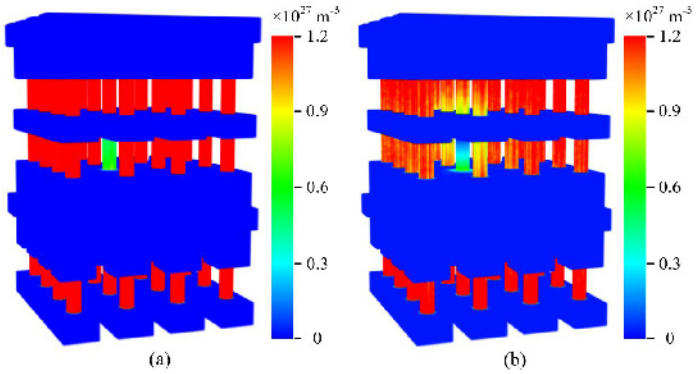

Figure C10 3-D ion density distributions in the CRRAM arrays (a) with high thermal resistance box at $t = 0.12s$ and (b) with no high thermal resistance box at $t = 0.4s$.

References

1 Kim S, Kim S J, Kim K M, et al. Physical electrothermal model of resistive switching in bi-layered resistance-change memory. Sci Rep, 2013, 3: 16890

2 Kim S, Choi S, Lu W. Comprehensive physical model of dynamic resistive switching in an oxide memristor. ACS Nano, 2014, 8: 2369-2376

3 Larentis S, Nardi F, Balatti S, Gilmer D C, Ielmini D. Resistive switching by voltage-driven ion migration in bipolar RRAM-Part II: Modeling. IEEE Trans Electron Dev, 2012, 59: 2468-2475

4 Snyder G J, Christensen M, Nishibori E, Caillat T, Iversen B B. Disordered zinc in Zn 4 Sb 3 with phonon-glass and electron-crystal thermoelectric properties. Nature Mater, 2014, 3: 458-463

5 Li D, Hng H H, Ma J, Qin X Y. Effects of Nb doping on thermoelectric properties of Zn4Sb3 at high temperatures. J Mater Res, 2009, 24: 430-435

6 Griffin A J, Brotzen F R, Loos P J. The effective transverse thermal conductivity of amorphous Si3N4 thin films. J Appl Phys, 1994, 76: 4007-4011

7 Ansari S U, Hussain M, Mazhar S, et al. Mesh partitioning and efficient equation solving techniques by distributed finite element methods: A survey. Arch Comput Methods Eng, 2019, 26

8 Wang D W, Chen W, Zhao W S, et al. An improved algorithm for drift diffusion transport and its application on large scale parallel simulation of resistive random access memory arrays. IEEE Access, 2019, 7: 31273-31285

9 International Roadmap for Devices and Systems: Beyond COMS, IEEE, 2017

10 Luo Q, Xu X, Liu H, et al. Super nonlinear RRAM with ultra-low power for 3D vertical nano-crossbar array. Nanoscale, 2016, 8: 15629-15636

11 Li K S, Ho C H, Lee M T, et al. Utilizing Sub-5 nm sidewall electrode technology for atomic-scale resistive memory fabrication. IEEE Symp VLSI Technol, Honolulu, HI, USA, 2014

12 Kurotsuchi K, Sasago Y, Yoshitake H, et al. 2.8-GB/s-write and 670-MB/s-erase operations of a 3D vertical chain-cell-type phase-change-memory array. IEEE Symp VLSI Technol, Kyoto, Japan, 2015: 92-93